crystals

MDPI

Article

Kinetics of Oxidation at High Temperature and Degradation States of Cr-Free Al-Containing Cobalt and Nickel Alloys Reinforced by TaC Carbides

Patrice Berthod [1,2]

[1] CNRS, IJL, Université de Lorraine, F-54000 Nancy, France; patrice.berthod@univ-lorraine.fr; Tel.: +33-3-72-74-27-29
[2] CNRS, FST, Université de Lorraine, F-54500 Vandoeuvre-lès-Nancy, France

Abstract

Two cobalt alloys and one nickel alloy, containing Ta and C in similar atomic contents and either 5 or 10 wt.% Al, were cast. Their microstructures and their oxidation behaviors in air at 1200 °C over 50 h were investigated. All contained eutectic script-like TaC carbides and a dendritic matrix which was either single-phased (FCC) or double-phased (FCC + Co_3Al). The cobalt sample with 5 wt.% oxidized catastrophically, became thinner, lost all its TaC, and was covered by a thick oxide shell (outer CoO and inner mixture of CoO, $CoAl_2O_4$ and Ta-rich oxides). The two other alloys, Ni-based with 5 wt.% Al and Co-based with 10 wt.% Al, oxidized more slowly, with a mass gain kinetic slightly lower than that for chromia-forming alloys at 1200 °C and a continuous duplex oxide scale made of an outer MAl_2O_4 spinel and inner Al_2O_3 scales. This evidences the existence of two Al content thresholds, depending on the base element, that must be exceeded to obtain acceptable oxidation behavior.

Keywords: cobalt-based alloys; nickel-based alloys; aluminum; Ta carbides; high temperature oxidation; thermogravimetry; metallographic characterization

1. Introduction

Metallic components working at around 1000 °C or more (hot elements of combustion turbines, glass-forming tools…) are generally threatened by deformation/rupture [1] and by chemical degradation due to their exposure to aggressive gas mixtures or molten substances [1,2]. Mechanical stresses, induced by fluid pressure or centrifugal forces, may significantly alter geometry and, thus, the function expected for the component (e.g., trajectory of combustion gas flows and, thus, the output of the mechanical power retrieved by the turbine, breakdown of blades…) [1,3]. Hot corrosion by gaseous or liquid fluids (combustion gases, molten sulfates and CaO–MgO–Al_2O_3–SiO_2 (CMAS) mixtures, molten glasses in some industries) also take part in the degradation of the component, notably by helping the mechanical loading for crack initiation and propagation.

For these reasons, these metallic components are generally made of nickel-based or cobalt-based superalloys, which are refractory enough and contain Ni or Co in rather high proportions, elements still easily available and easy to cast. These superalloys benefit from the introduction of particular elements to enhance the resistance against the mechanical and chemical solicitations described above. They can also benefit from external thermal insulation coatings associated with internal cooling solutions to prevent

Check for updates

Academic Editor: Shouxun Ji

Received: 23 December 2025
Revised: 26 January 2026
Accepted: 5 February 2026
Published: 8 February 2026

Copyright: © 2026 by the author. Licensee MDPI, Basel, Switzerland. This article is an open access article distributed under the terms and conditions of the Creative Commons Attribution (CC BY) license.

too high temperatures experienced by the alloy. An increase in the resistance against creep can be achieved by modern solutions such as the very efficient single-crystalline solidification associated with the precipitation of reinforcing intermetallic particles (namely gamma prime—$Ni(Co,Fe)_3Al(Ti,Ta,Nb)$—precipitated in high-volume fractions) [1,4] or coarse-grained Ni or Fe alloys strengthened by fine and homogeneous dispersion of Y_2O_3 nano-oxides (Oxide Dispersion-Strengthened superalloys) [1]. Unfortunately, the use of single crystals is limited to 1100 °C because instability of the gamma prime precipitates occurs, leading to possible total disappearance beyond 1100 °C. These alloys are also limited to particular geometries (elongated components such as turbine blades), a problem which also affects O.D.S. alloys, the structures of which are anisotropic (in one or two dimensions).

More freedom in geometric design is possible with polycrystalline equiaxed alloys (casting, powder metallurgy, additive manufacturing), but equiaxed granular structures coarse enough to favor mechanical strength for elevated temperatures are accessible only by casting. However, coarse grains are not enough, and other solutions need to be additionally applied such as solid solution strengthening and precipitation (during solidification and/or solid-state high-temperature isothermal stages) of hard particles with favorable geometry, size and repartition. By adding the condition of high stability at elevated temperatures, monocarbides (MCs) appear as a good choice, notably tantalum mono-carbides (TaCs).

TaC is a key particle to strengthen superalloys. It has been known for a long time [5], notably when present in important proportions in some famous superalloys such as Mar-M509 [6,7]. Generally, these alloys (principally cobalt-based) have oxidation and corrosion resistance based on the presence of chromium [8]. Aluminum, the other element playing a very important role in resistance to oxidation, is most often absent in superalloys strengthened by carbides. Al is generally present in most nickel-based alloys [1,4]. Al can also be encountered in a series of cobalt-based alloys containing Ta [9–12], high-entropy alloys [13], or Co-containing Ta-based refractory alloys [14], but essentially in C-free alloys, even if some rare exceptions can be noticed, as in some directionally solidified cobalt alloys (e.g., [15]) or in high-entropy alloys (e.g., [16]).

To summarize, 1. Ni and Co are base elements which allow for elaborating polycrystalline coarse-grained superalloys with large shape freedom rather easily by foundry; 2. TaC is an efficient particle for resisting creep at temperatures beyond 1100 °C and 1200 °C, for instance (stable enough, in contrast with gamma prime or chromium carbides); and 3. alumina is a stoichiometric oxide which limits anionic and cationic diffusion, grows slowly (in contrast with the not really stoichiometric chromia) and is not re-oxidable in volatile species (in contrast with chromia, which is re-oxidized into gaseous CrO_3 when $T > 1000$ °C).

Thus, alumina-forming Co-based or Ni-based alloys strengthened by TaC carbides represent a very interesting potential base for the development of new superalloys more performant at elevated temperatures. Curiously, it seems that no published articles deal with such a metallurgical principle. The aim of the present work is precisely to start investigating the possible microstructures and oxidation properties of cobalt and nickel alloys containing TaC to resist creep and aluminum to resist oxidation.

2. Materials and Methods

2.1. Choice of the Alloys and Elaboration

Three alloys were defined to start exploring the characteristics which may result from the simultaneous presence of Al and TaC in a cobalt or nickel alloy possibly representing a base for developing real superalloys. They were Ni(bal.)–5Al–0.4C–6Ta (“NACT5”), Co(bal.)–5Al–0.4C–6Ta (“CACT5”) and Co(bal.)–10Al–0.4C–6Ta (“CACT10”), with all contents in wt.%.

All alloys were obtained by melting pure Ni or Co, Al, C and Ta. These elements were introduced in the charges as metallic flakes and graphite rod (Alfa Aesar, Haverhill, MA, USA) with purity > 99.9%). Melting and the following solidification were done in a 50 kW induction furnace (CELES, Lautenbach, France). As a gaseous atmosphere, the fusion chamber, closed with a silica tube, contained 800 mbar of pure argon. The input voltage was increased to the maximal value of 5 kV, while the alternative current (4 A) stayed at the 100 kHz frequency. Solidification led to solid compact ingots weighing about 40 g in each case.

2.2. Obtained Chemical Compositions and As-Cast Microstructures

The obtained ingots were cut into several parts using a metallographic saw. For each alloy, a first part was embedded in resin, ground with SiC papers (grade from #240 to #1200), washed, and finally polished (textile disk supporting 3 μm hard particles).

The microstructures of the metallographic samples, with a mirror-like surface, were examined using a Scanning Electron Microscope (SEM). This one (model: JSM 6010LA, manufacturer: JEOL, Tokyo, Japan) was used with a 20 kV acceleration voltage, and the imaging mode was Back Scattered Electrons (BSE).

The chemical compositions were analyzed by Energy Dispersion Spectrometry (EDS) using the spectrometer attached to the SEM. Although EDS is a semiquantitative technique, the EDS spectrometer (JEOL, Tokyo, Japan) used here gives accurate results (better than $\pm$0.5 wt.%), close to Wavelength Dispersion Spectrometers. This was performed on five $\times$250 areas randomly chosen in the bulk. With this EDS device, the accuracy of the values obtained for each content was about $\pm$0.2 wt.%. The average value and the standard deviation values were calculated from these five obtained results.

2.3. Oxidation Tests

Since it is hoped that these new systems, on the one hand, will still allow strengthening phases (TaC) to be present at temperatures beyond 1100 °C (unlike the gamma prime precipitates of the Ni-based single crystals), and on the other hand, will have an alumina scale much more efficient than chromia against oxidation at such elevated temperatures, 1200 °C was chosen to test the behaviors of these new alloys during exposure to both heat and oxidation. The oxidation tests were, thus, carried out at 1200 °C, for 50 h, in a thermo-balance TGA92 (manufacturer: SETARAM, Caluire, France) in a 1.5 L/h flow of synthetic air. Heating to 1200 °C was performed at +20 °C min^{-1}, and the final cooling was done at −5 °C min^{-1}. The oxidation samples were parallelepipeds with the following approximate dimensions: 3 mm × 3 mm × 10 mm. Their six faces were ground using #1200 SiC papers. Edges and corners were smoothed (using the same grade of SiC paper). The mass gains were plotted versus time for the isothermal stage to specify the kinetics of oxidation at 1200 °C. Mass variation was also plotted versus temperature for the whole cycle to obtain Supplementary Data on the heating part and on the cooling part.

2.4. Characterization of the Oxidized States

The oxidized surfaces of the samples were first observed with the SEM in Secondary Electrons (SE) imaging mode, and second subjected to elemental EDS mapping. They were thereafter embedded in the same resin system as the metallographic as-cast parts, then divided into two halves using the metallographic saw. The obtained metallographic samples were ground and polished to obtain a mirror-like state for cross-sectional observation. The external and internal oxides, as well as the subsurfaces affected by oxidation, were observed with the SEM in BSE mode. EDS elemental mapping and EDS spot analyses helped to identify the oxide natures and to specify the chemical composition in the subsurfaces.

3. Results and Discussion

3.1. Chemical Compositions of the Alloys

The chemical compositions of the three alloys in their as-cast states are displayed in Table 1. The Al contents are slightly lower than the targeted ones (about 0.5–1 wt.% less for the expected 5 wt.% Al, about 1–1.5 wt.% less for the expected 10 wt.% Al). This can be explained by the high reactivity of this element, which led to oxidation of a part of the aluminum by the oxygen and nitrogen traces necessarily present in the "pure" argon occupying the melting chamber (the volume of which is more than 1 L). A partial sublimation of this element, which melts at 660 °C only and vaporizes at 2470 °C, may also lead to a small loss. Such phenomena are well known and they are reported in a series of more or less recent articles (e.g., [17–21]).

Table 1. Chemical compositions of the three alloys in their as-cast states (wt.%, SEM/EDS; five ×250 full-frame analyses).

wt.%	Ni or Co	Al	Ta	C
NCAT5	Ni(bal.)	4.6 ± 0.2	7.5 ± 0.6	Not measurable
CACT5	Co(bal.)	4.1 ± 0.1	7.9 ± 0.2	Not measurable
CACT10	Co(bal.)	8.8 ± 0.2	5.3 ± 0.5	Not measurable

In contrast, the Ta content determined by EDS seems a little higher than the targeted one, a phenomenon seen by other researchers. This can be explained by the probable presence of many TaCs in relief on the surface after finishing polishing, due to the high hardness of this compound; overestimation of Ta is frequently seen when EDS is used. Globally, it can be considered that the desired chemical compositions were rather respected.

3.2. As-Cast Microstructures of the Alloys

The microstructures in as-cast condition are illustrated in Figure 1 by SEM/BSE micrographs. The three alloys are composed of a dendritic matrix and an interdendritic network of script-like shaped tantalum carbides. These are essentially of a eutectic nature, as suggested by their multi-elongated shape mixed with the matrix, but some rare coarse TaC can also be seen here and there.

The matrixes of the NACT5 and CACT5 alloys contain all the aluminum, and a part of tantalum, which is higher in the matrix for NACT5 (≅5 wt.% Ta) than for CACT5 (≅2 wt.% Ta). This is logical, since the TaC phase is more present in the cobalt alloy than in the nickel alloy. The matrix of the CACT10 alloy is clearly double-phased: about a clear half is with the approximately 7 wt.% Al–2 wt.% Ta composition and the second half—much darker—contains 13 wt.% Al–2 wt.% Ta. These two cobalt-based parts of the matrix seem to be Al-saturated for the clear one and close to the Co_3Al intermetallic for the dark one (a Ta-containing version of the Co_3Al intermetallic compound). To our knowledge, there is no thermodynamic description for the Co-Al-Ta-C quaternary system. However, ternary Co-Al-Ta was investigated recently, and a mix of the FCC cobalt solid solution and the Co_3Al intermetallic (also containing a little fraction of Ta) is expected in the isothermal triangular sections between 1000 °C and 1300 °C [22].

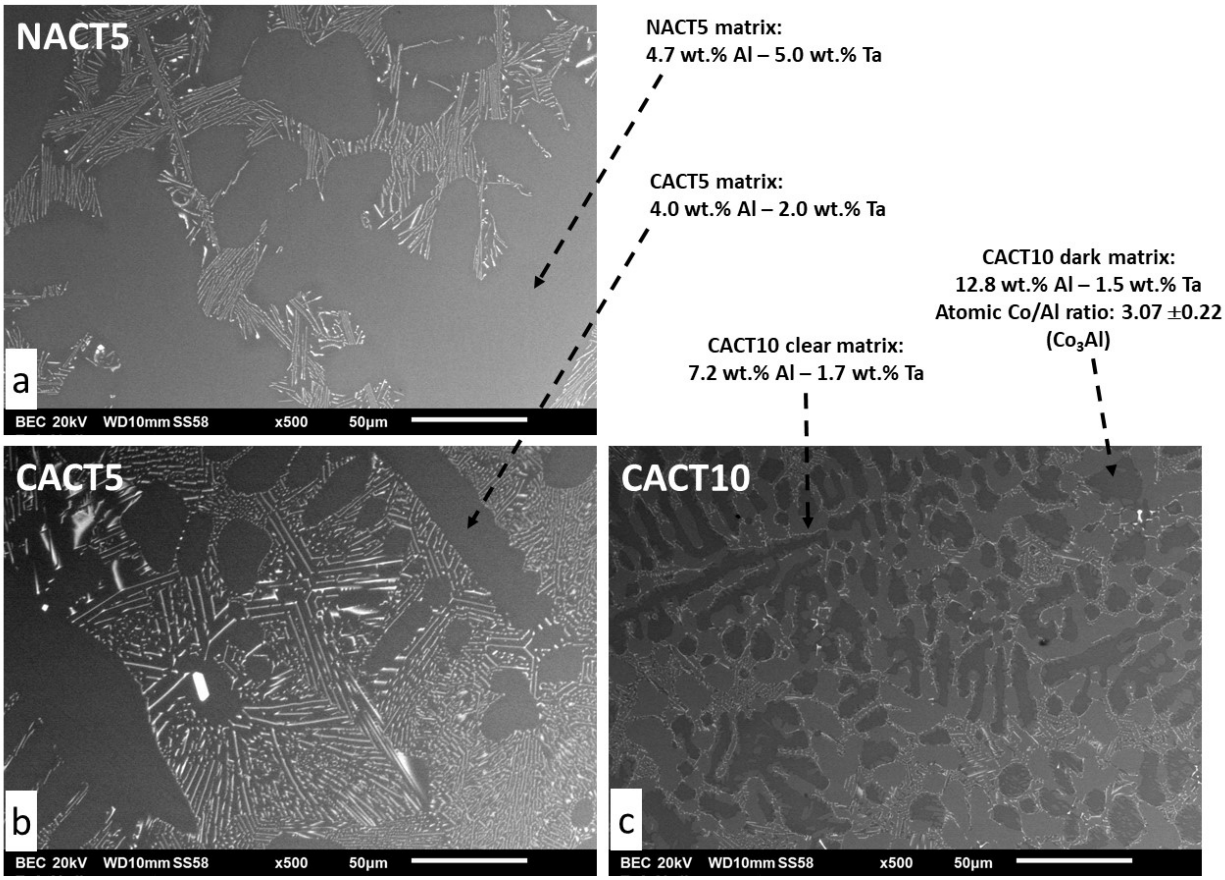


Figure 1. Microstructures of the three alloys: (**a**) NACT5 (Ni-5Al-0.4C-6Ta), (**b**) CACT5 (Co-5Al-0.4C-6Ta) and (**c**) CACT10 (Co-10Al-0.4C-6Ta).

3.3. Isothermal Oxidation Kinetics

The isothermal mass gain curves obtained for the three alloys are plotted together in Figure 2. It can be noticed first that the mass gain by oxidation of CACT5 is parabolic but particularly rapid. It oxidizes much faster than the NACT5 and CACT10 alloys, the curves of which are repeated in Figure 3 at a more favorable vertical scale for better readability.

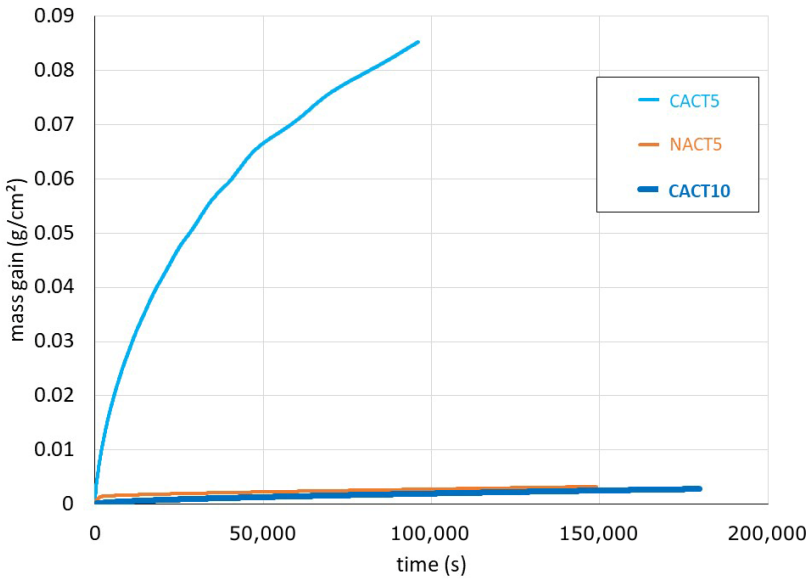


Figure 2. Mass gain curves during oxidation of the three alloys at 1200 °C.

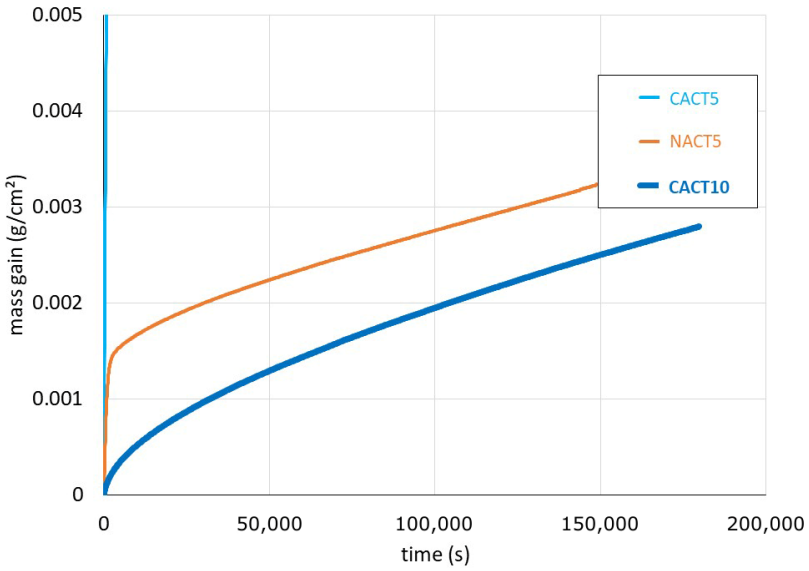


Figure 3. Vertical enlargement of the mass gain curves of CACT10 and NACT5.

The mass gain curve of NACT5 starts with an important linear oxidation before becoming parabolic (transient oxidation), while the mass gain kinetic of CACT10 is parabolic as soon as the temperature reaches 1200 °C. It can be said, before confirmation by metallographic characterization, that 10 wt.% Al allowed CACT10 to be covered by an efficient protective oxide scale, maybe alumina, while the NACT5 alloy was itself protected by such a protective scale but after a short delay. Concerning the CACT5 alloy, the parabolic but extremely fast oxidation kinetic suggests that other elements than aluminum were oxidizing. Taking the mass gain during heating (CACT5 and CACT10), with addition of transient oxidation in the case of the NACT5 alloy, the isothermal mass gains were treated according to a method allowing better representativity of the parabolic constant Kp. Table 2 gives the obtained values, which show that the Kp of CACT5 is one thousand times higher than that for the two other alloys, the Kp values of which are equivalent to one another.

Table 2. Values of the parabolic constants.

Alloy	Kp ($\times 10^{-12}$ g^2 cm^{-4} s^{-1})
NACT5	≅42
CACT5	≅46,000
CACT10	≅39

3.4. Mass Variations During Heating and Cooling

The mass gain during heating, after correction for the air buoyancy variation (Archimede's pressure decrease), is plotted for the three alloys together in Figure 4. This suggests that oxidation started to be detectable by the thermobalance for temperatures which were lower for the two cobalt alloys (≅400 °C) than for the nickel one (≅550–600 °C). This shows that CACT5 and CACT10 are more reactive than NACT5. The characterization of the oxides may allow for interpreting these differences.

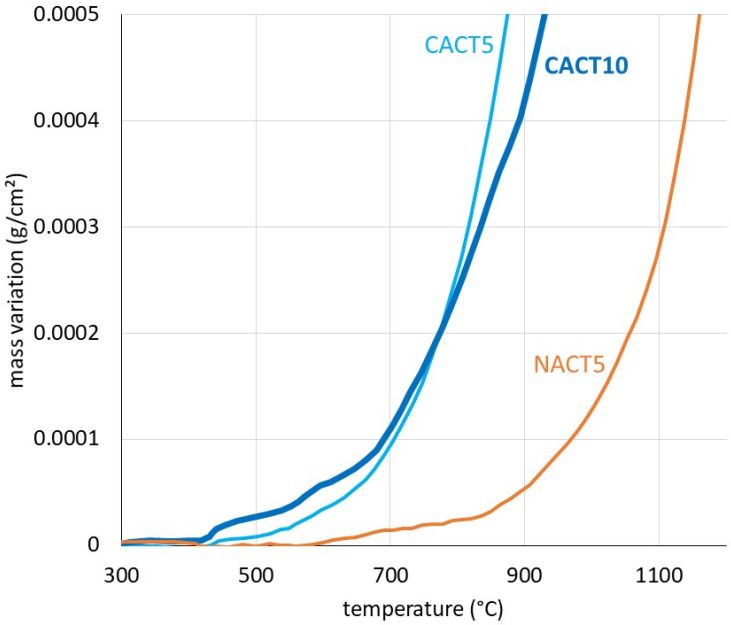


Figure 4. Start of mass gain by oxidation during heating.

Similarly, the mass variation was studied versus temperature during cooling. The obtained curves, plotted together in Figure 5, show—for the CACT10 alloy—a slow mass decrease due to air buoyancy variation, then the start of mass loss due to oxide scale spallation, which seems to occur later for the CACT10 cobalt alloy (≅350 °C) than for the NACT5 nickel alloy (≅500 °C), which lost more oxide (negative mass variation along the whole thermal cycle). Concerning the CACT5 cobalt alloy, it did not face the problem of oxide detachment during cooling. Here too, we will wait for the metallographic post-mortem analysis to try to explain these differences in behavior.

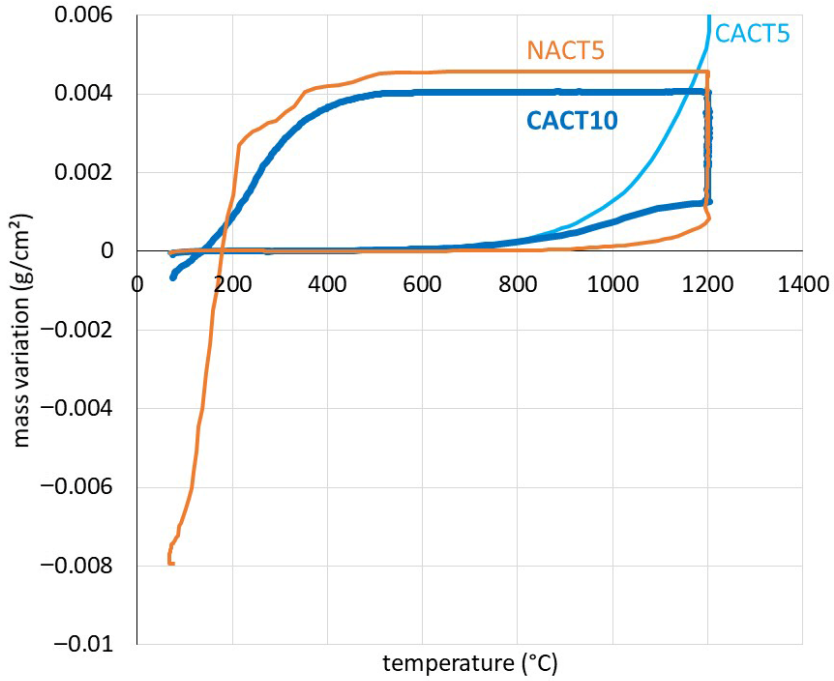


Figure 5. Oxide scale spallation evidenced in the cooling parts of the mass variation curves of the NACT5 and CACT10 alloys throughout the whole thermal cycle (isothermal oxidation and cooling not represented for CACT5 because of too-great mass gains).

3.5. Aspects of the Oxidized Surfaces

With the naked eye and the SEM at low magnification in SE mode (Figure 6a), it is visible that the CACT5 alloy is covered all around by a thick oxide shell, the outermost part of which is the cobalt oxide CoO, as identified by EDS. Its polycrystalline structure (Figure 6b) and its porous texture (Figure 6c) can be observed. It is well known that the cobalt oxide, which is not stoichiometric, unlike alumina (and even chromia), is not protective. Here, in addition, the fact that the CoO oxide formed on the CACT5 alloy is porous decreases its protective effect a second time. It is, thus, not surprising that the oxidation kinetic was so fast.

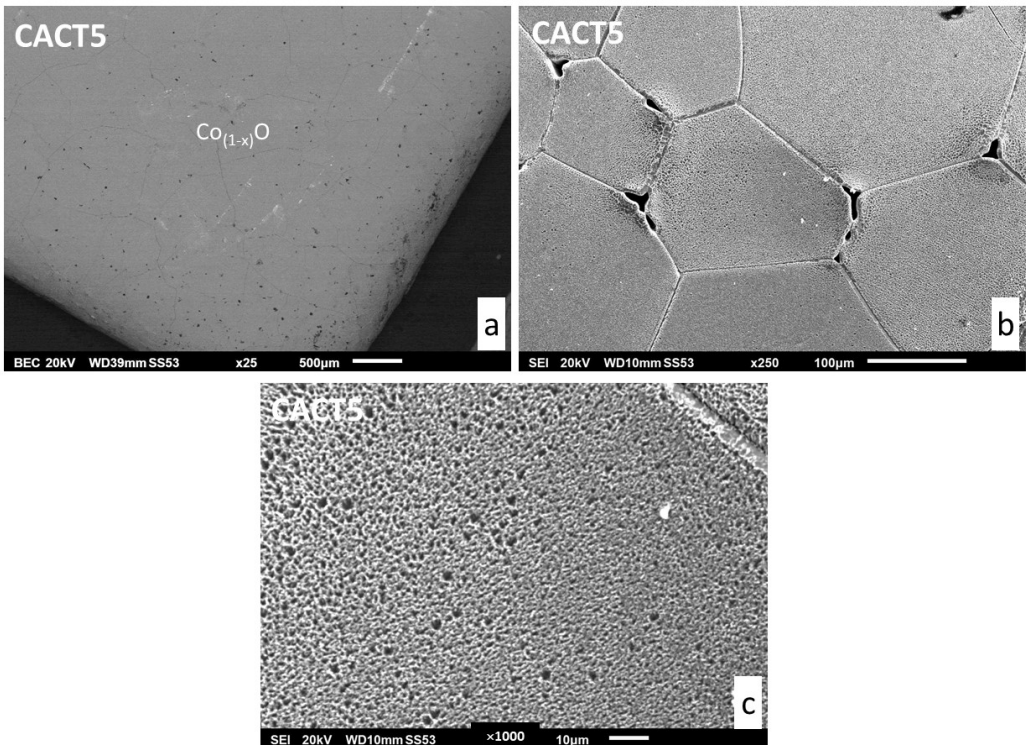


Figure 6. SEM/SE observation of the oxidized CACT5 alloy at low (**a**), medium (**b**) and high (**c**) magnification.

In contrast, with 5 wt.% more Al, the CACT10 alloy behaved much better, according to the slow mass gain kinetic. Unlike that of the CACT5 alloy, the post-isothermal cooling of the CACT10 alloy induced oxide spallation (Figure 5). The loss of parts of the external oxides here and there allows for examining the structure of the oxide scale in its depth, from the outer face of the scale to the alloy surface (bright in the SEM/BSE micrograph, Figure 7). Spot analyses allow for identifying the gray outermost part of the scale as being an oxide of both cobalt and aluminum (possibly the $CoAl_2O_4$ spinel oxide) and the innermost dark part of the scale as being alumina (Figure 7). The EDS elemental map given in Figure 8 confirms that the bright areas are the denuded alloy, the dark areas are alumina (innermost layer) and the gray areas are the oxides of both Co and Al (outermost layer). The external oxide scales for the NACT5 alloy are similar (Figure 9): denuded alloy regions, dark areas of alumina (innermost layer), and gray areas of oxides of both Ni and Al (outermost layer).

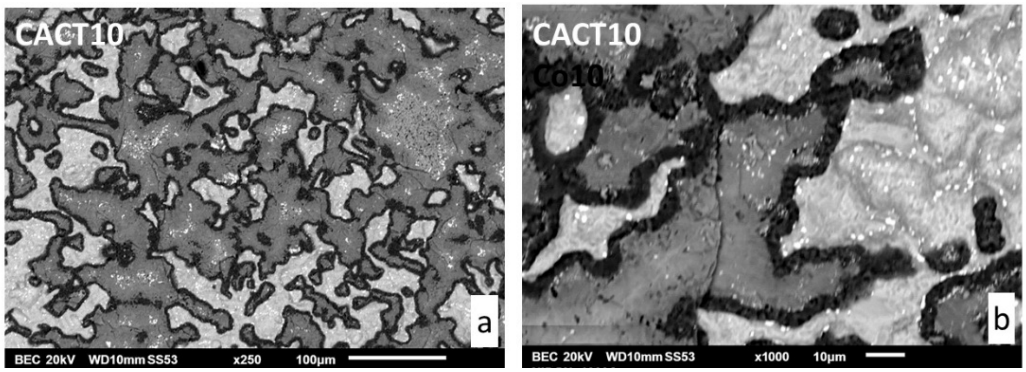


Figure 7. Low- (**a**) and high- (**b**) magnification views of the parts of oxide scale remaining after spallation during cooling (SEM/BSE).

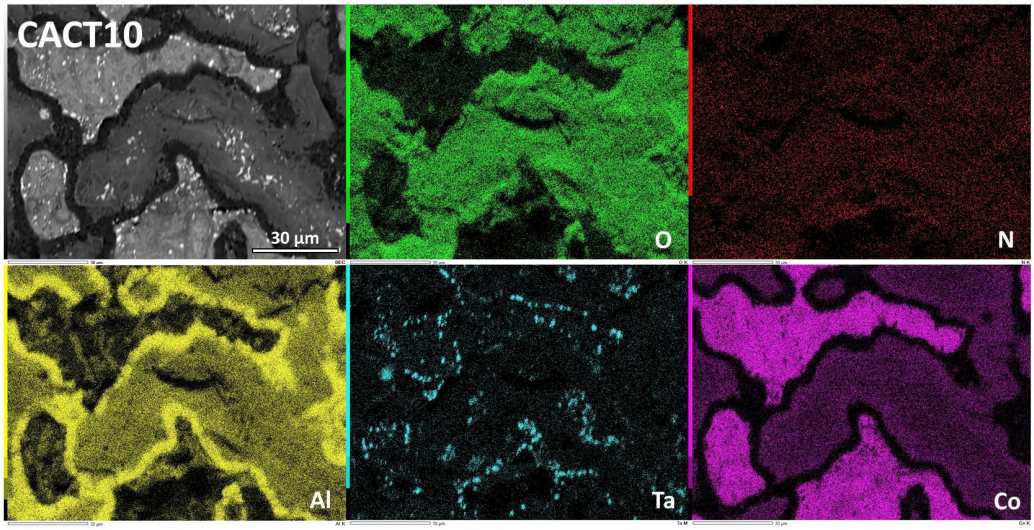


Figure 8. Elemental EDS map helping to identify the different parts of the external scale (here: CACT10).

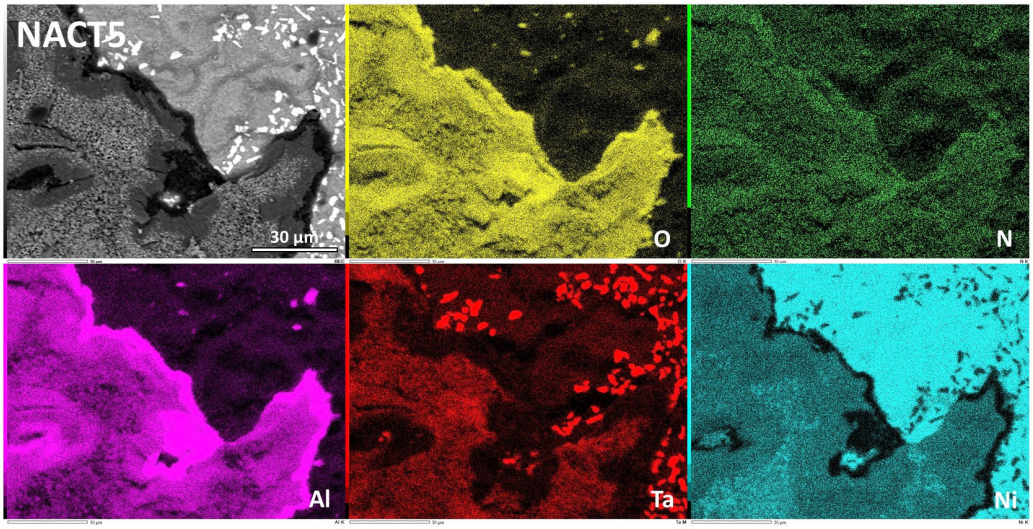


Figure 9. Elemental EDS map helping to identify the different parts of the external scale (here: NACT5).

3.6. Cross-Sectional Observations of the Catastrophically Oxidized CACT5

After embedding, cutting and grinding/polishing, the obtained mirror-like metallographic samples of the oxidized alloys allowed for observing the oxide scales and the subsurface deterioration in depth.

Figures 10–12 describe the oxidized CACT5. Figure 10 contains a general view of the oxidized sample, with delimitation of the following map (dotted rectangle), and the EDS map of the innermost oxide and the interface with the alloy. Figure 11 represents the same general view, with a dotted square delimiting the following EDS map, and this high-magnification EDS map of the innermost oxide. Figure 12 (SEM/BSE) presents micrographs of the outermost CoO oxide and the innermost oxide mixture, an EDS line scan across the whole oxide scale (in atomic percent to evidence the oxide types) and an EDS line scan (in weight percent) across the whole thickness of the remaining alloy.

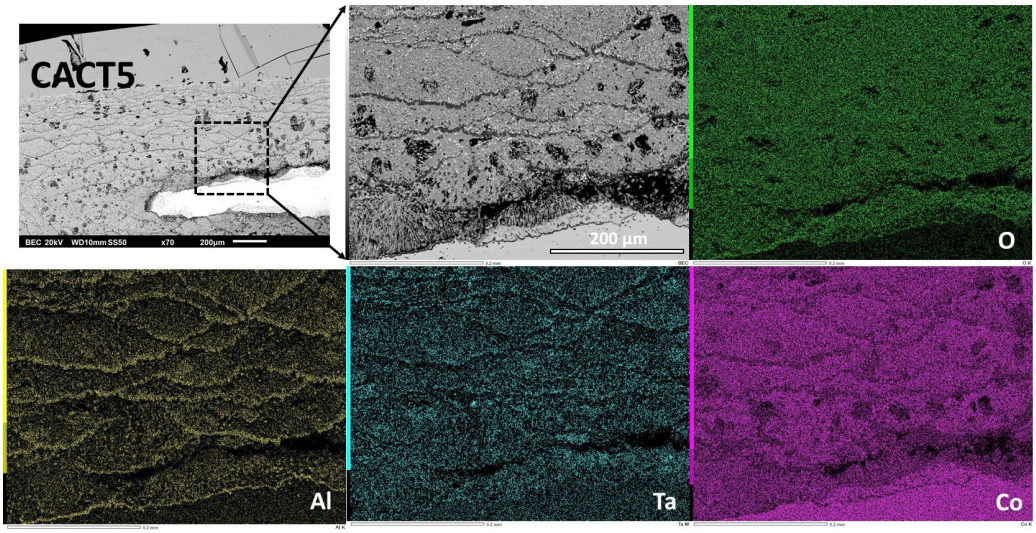


Figure 10. Elemental EDS map on the oxide scale and deteriorated subsurface of the CACT5 alloy, at low magnification.

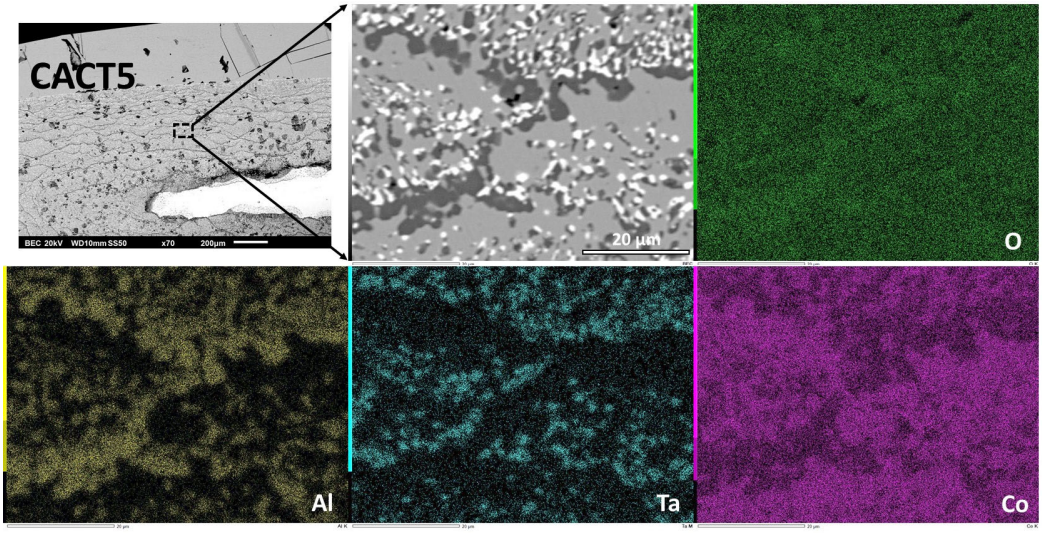


Figure 11. Elemental EDS map on the innermost part of the oxide scale covering the CACT5 alloy, at high magnification.

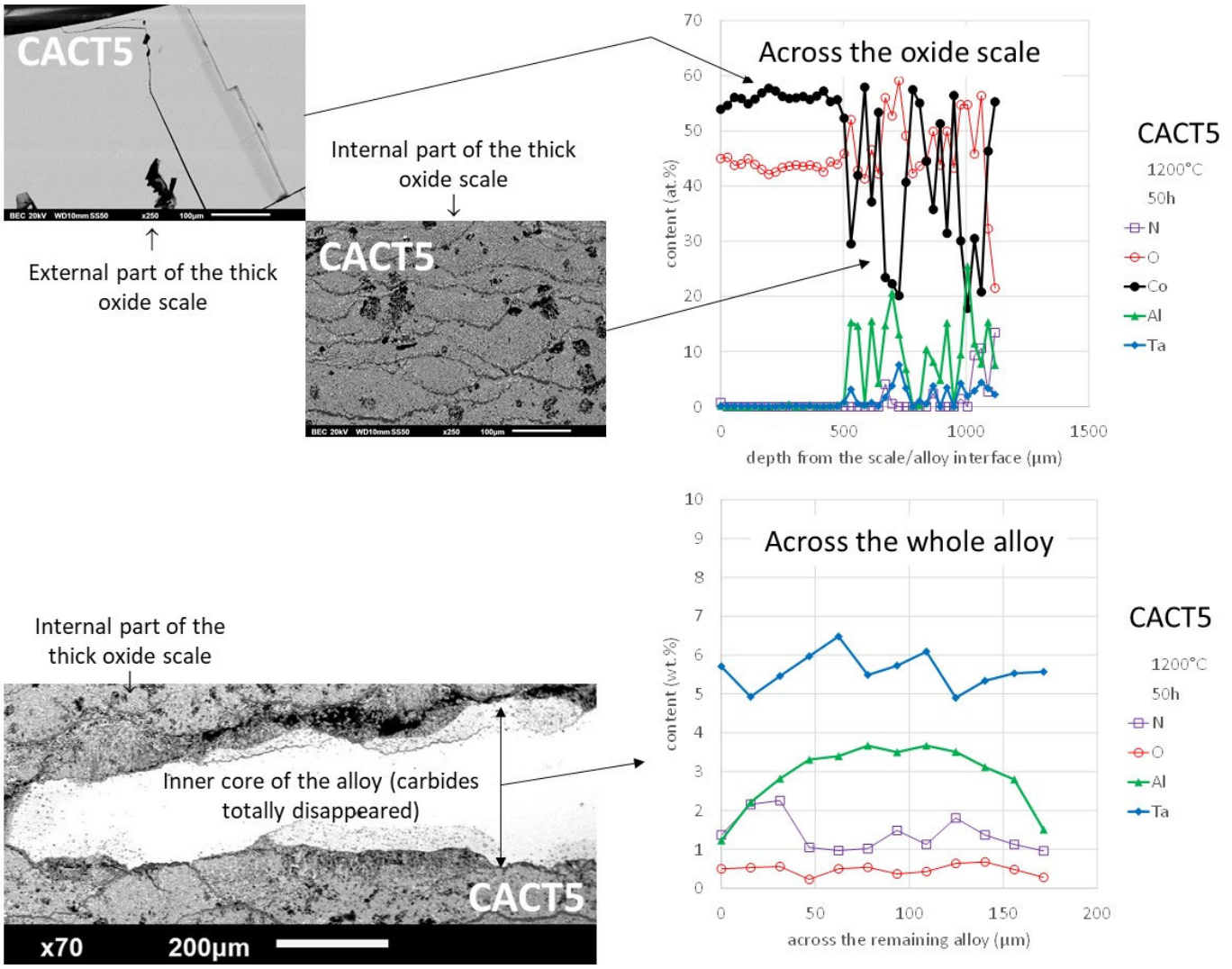


Figure 12. Oxidized CACT5 alloy: SEM/BSE micrographs and EDS line scan across the whole oxide scale (two zones) and across the whole remaining alloy.

The SEM/BSE micrographs present in Figure 10 and in Figure 11 show that the external oxide scale is particularly thick and composed of two distinct layers: a 400 µm thick outermost layer of cobalt oxide and a 600 µm thick innermost layer of complex oxide. As seen above with the surface observation of the oxidized sample for another orientation (Figure 6a,b), the outermost cobalt oxide is coarse-grained, while the innermost complex oxide is poly-phased (mix of gray oxide, dark oxide and bright oxides) with a finer structure, appearing stratified. The EDS line scan (Figure 12, top) reveals, after the almost constant contents in Co and O across the outermost coarse-grained oxide, high variations in all elements across this innermost part of the scale. For more details about the external oxides, EDS spot analysis was carried out on the different oxides belonging to the external scale observed in cross-sections. The results displayed in Table 3 confirm that the thick outermost part of the scale is CoO, while this oxide is also present in the thick innermost part of the scale, mixed with the $CoAl_2O_4$ spinel and with dispersed Ta-rich oxides too fine to be analyzed with accuracy.

Table 3. Chemical compositions of the different oxides present (SEM/EDS, spot analyses).

CACT5 Alloy (Contents in at.%)	O	Al	Co	Ta
Outermost part of the oxide scale (gray when observed by SEM/BSE) **$Co_{1+x}O$**	43.6 ± 0.8	0.22 ± 0.1	56.2 ± 0.9	0.1 ± 0.1
Poly-phased innermost part of the oxide scale; dark part when observed by SEM/BSE **$CoAl_2O_3$**	51.3 ± 0.7	29.8 ± 0.9	18.9 ± 1.6	/
Poly-phased innermost of the oxide scale; gray part when observed by SEM/BSE **$Co_{1+x}O$**	42.5 ± 0.8	0.1 ± 0.1	57.4 ± 0.7	0.1 ± 0.1
Poly-phased innermost of the oxide scale; clear when observed by SEM/BSE	Too fine to be analyzed; rich in Ta			

This particular structure suggests an inwards progress of oxidation. At first, cobalt was the main element to be oxidized (outermost CoO oxide), despite the presence of aluminum, which is more oxidable but was not present in a high enough content. Later, aluminum started to take part in oxidation, which led to the formation of the $CoAl_2O_4$ spinel. The consumption of Al induced a decrease in Al content and CoO formed again. Oxidation oscillated between oxidation of Co only (with consequent re-enrichment in Al) and oxidation of both Co and Al (with consequent impoverishment in Al), and oxide growth progressed wave by wave, resulting in the stratified constitution of the complex innermost oxide scale. The consumption of aluminum to form the $CoAl_2O_4$ spinel, alternated with CoO, is visible in Figure 12 in the EDS line scan acquired across the whole thickness of the remaining alloy (which was itself also consumed by oxidation). This EDS line scan shows clearly on both sides the diffusion of Al towards the oxidation front moving inwards. This Al feeding of the oxidation front was never sufficient to allow the development of a continuous alumina scale or a continuous $CoAl_2O_4$ spinel scale. This explains the general oxidation of the alloy and the associated fast mass gain.

The total disappearance of carbides demonstrates that carbon also diffused towards both oxidation fronts to be oxidized into gases. The resulting impoverishment of the matrix surrounding the TaC carbides destabilized these carbides, and they dissolved to feed the matrix in carbon, which thereafter diffused towards the oxidation fronts. In contrast, the tantalum atoms released by the dissolving TaC carbides stayed where they were and did not diffuse, as shown by the Ta EDS line scan across the remaining alloy (Figure 12).

It can be thought that, if the oxidation duration was longer, the alloy should be totally transformed into a mixture of oxides looking like the innermost part of the oxide shell formed all around the sample.

3.7. Cross-Sectional Observations of the Moderately Oxidized NACT5

Although its Al content was the same as that of the CACT5, the nickel alloy NACT5 behaved much better in oxidation. The external oxide scale was made of an outermost $(Ni, Al)_xO_y$ oxide and an innermost aluminum oxide (Figure 13). EDS spot analysis allowed for specifying the $(Ni, Al)_xO_y$ composition, which is not really the $NiAl_2O_3$ spinel, as thought above. Indeed, it is a nickel aluminum oxide with variable composition (Figure 14). Towards the interface with the alloy, the content of Ni decreases and the content of Al increases. In contrast, the aluminum oxide is well identified as being alumina (Al_2O_3). Isolated nickel oxides and a thin complex oxide involving tantalum are present on the top of the spinel scale.

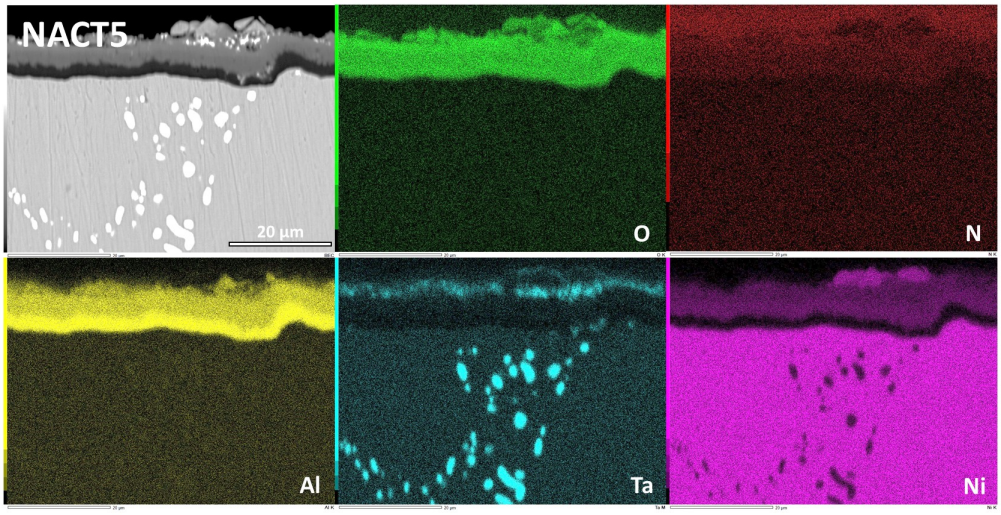


Figure 13. Elemental EDS map on the external oxide scale and the subsurface of the NACT5 alloy.

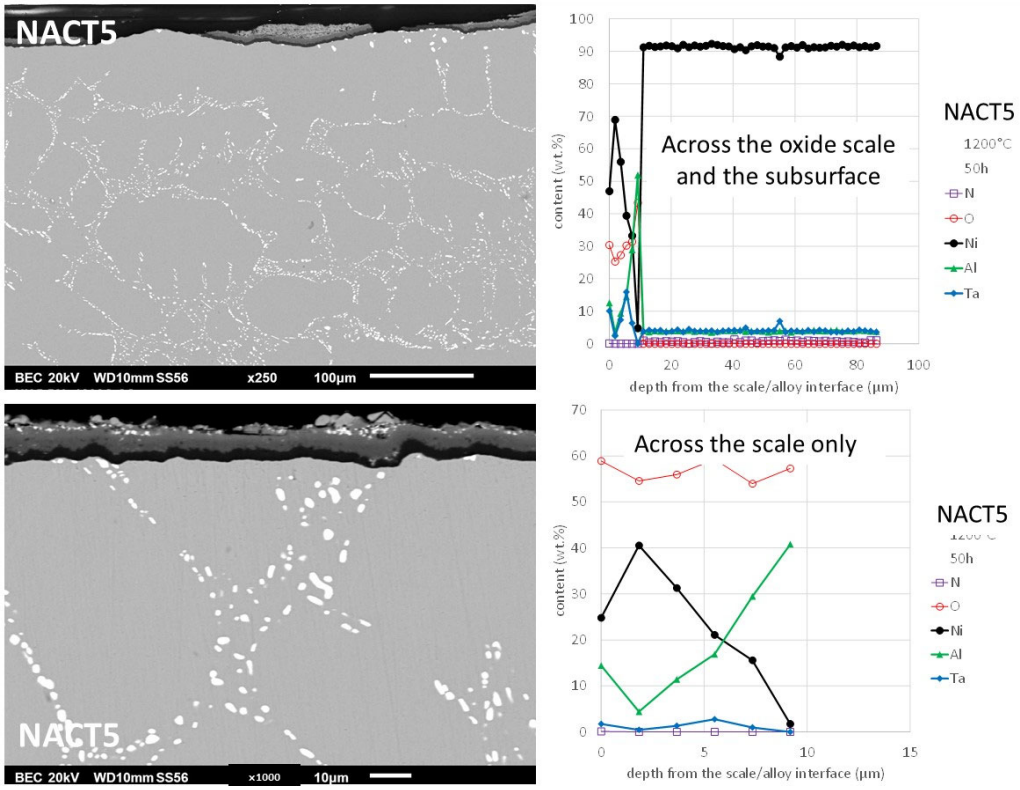


Figure 14. Oxidized NACT5 alloy: SEM/BSE micrographs and EDS line scan across the oxide scale and the subsurface (**top right**) and across the oxide scale only (**bottom right**).

Here too, to complete the oxide characterization, additional EDS spot analyses were performed on the different external oxides observed in cross-sections (Table 4). From the interface with the alloy to the interface with air, one finds Al_2O_3, the spinel $NiAl_2O_4$, a more oxygen-rich version of the spinel, and finally fractioned NiO particles. Similarly to the CACT5 alloy, oxidation started within a short duration of oxidation of nickel (the most abundant element present) into NiO prior to the selective oxidation of the more oxidable element Al into Al_2O_3. Due to the elevated temperature, NiO and Al_2O_3 reacted together to give the $NiAl_2O_4$ spinel. The innermost part of Al_2O_3, which formed a continuous and rather thick underlayer, acted thereafter as an efficient diffusion barrier which was at the origin of the slow mass gain and the moderate total thickness of the oxide scale.

Table 4. Chemical compositions of the different oxides present (SEM/EDS, spot analyses).

NACT5 Alloy (Contents in at.%)	O	Al	Ni	Ta
Outermost part of the oxide scale (fractioned, clear when observed by SEM/BSE): $\mathbf{Ni_{1-x}O}$	55.1 ± 1.5	0.9 ± 0.3	43.7 ± 1.8	/
Intermediate part of the oxide scale (gray when observed by SEM/BSE) $\mathbf{NiAl_2O_4}$	55.5 ± 1.0	30.4 ± 0.8	13.8 ± 1.0	0.9 ± 1.4
Innermost part of the oxide scale (dark when observed by SEM/BSE) $\mathbf{Al_2O_3}$	56.5 ± 0.9	42.3 ± 1.3	1.2 ± 0.5	/

In the subsurface, due to the protection conferred by the innermost alumina scale, no internal oxidation occurred; the subsurface and bulk microstructures were not affected by oxidation, only by exposure at high temperatures, which induced fragmentation and globularization of the TaC carbides. This phenomenon is common with {Ni–Cr} and {Co–Cr}-based superalloys reinforced with eutectic TaC carbides and is explained by the necessary decrease in the TaC/matrix interfacial energy, which becomes rapid at high temperatures.

3.8. Cross-Sectional Observations of the Moderately Oxidized CACT10

With 5 wt.% more Al than the CACT5 alloy, the CACT10 alloy behaved much better in oxidation, with a much slower mass gain rate and external hot corrosion products similar to the NACT5 alloy if one substitutes Ni with Co in the oxide formulas. Indeed, there is, on the surface of the CACT10 alloy, an outermost scale made of oxides of both Co and Al and an innermost aluminum oxide layer (Figure 15). The two EDS line scans (Figure 16) demonstrate that, across the thick oxides of Co and Al, the atomic contents of Co and of Al vary when moving towards the interface with the alloy (from Co-rich, Al-poor to Co-poor, Al-rich). According to the additional EDS spot analysis results acquired for better specifying oxides (Table 5), the average composition of the Co and Al oxides is close to the $CoAl_2O_4$ stoichiometry and the underlying oxide scale in contact with the alloy is Al_2O_3.

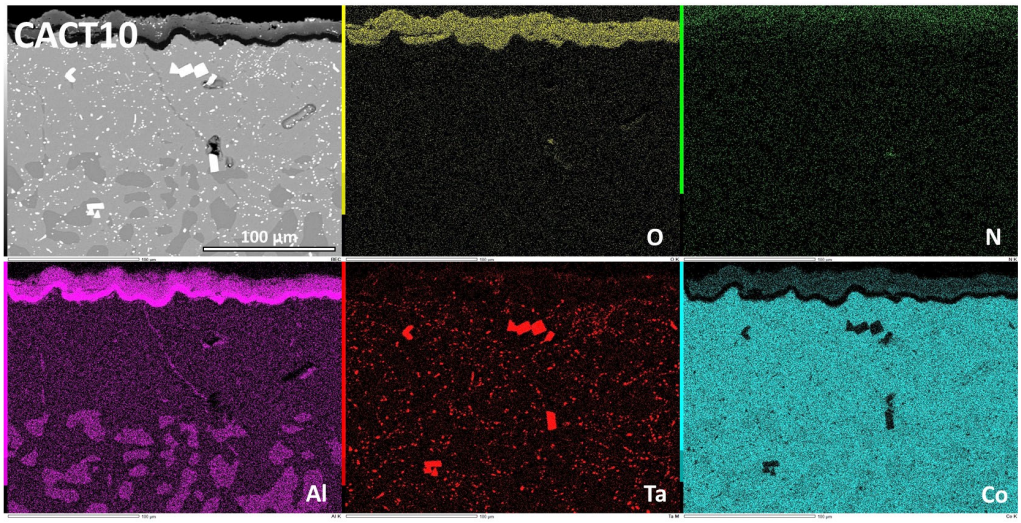


Figure 15. Elemental EDS map on the external oxide scale and the subsurface of the CACT10 alloy.

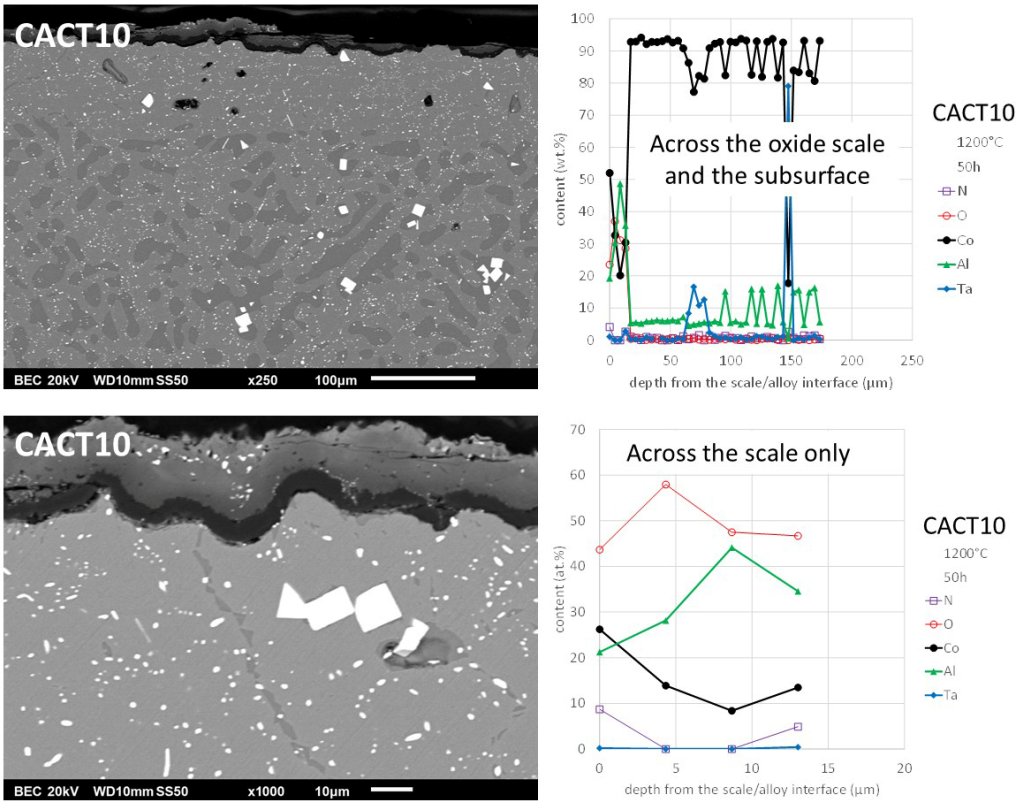


Figure 16. Oxidized CACT10 alloy: SEM/BSE micrographs and EDS concentration profiles across the oxide scale and the subsurface (**top right**) and across the oxide scale only.

Table 5. Chemical compositions of the different oxides present (SEM/EDS, spot analyses).

CACT10 Alloy (Contents in at.%)	O	Al	Co	Ta
Outermost part of the oxide scale (clear when observed by SEM/BSE) **Oxygen–rich $CoAlO_4$**	69.7 ± 3.0	20.4 ± 3.0	9.8 ± 0.2	/
Intermediate part of the oxide scale (gray when observed by SEM/BSE): **$CoAl_2O_4$**	54.9 ± 2.4	31.1 ± 2.7	14.1 ± 0.8	/
Innermost part of the oxide scale (dark when observed by SEM/BSE): **Al_2O_3**	56.8 ± 2.5	42.7 ± 2.3	0.6 ± 0.2	/

As seen above that the CACT5 alloy oxidized catastrophically, notably due to its inability to form a continuous alumina layer, either as a single oxide scale or as an underlying oxide layer. With 5 wt.% more Al, CACT10 succeeded in developing such a continuous alumina scale beneath a continuous $CoAl_2O_4$ spinel oxide. As for the NACT5 alloy, this double layer of continuous spinel superposed with a continuous alumina scale acted as an efficient barrier against the diffusion of the species involved in the oxidation phenomenon.

Another interesting observation concerns the modification of the subsurface: not only has its chemical composition been logically modified (e.g., gradient in Al concentration), but its microstructure has itself transformed. Indeed, the SEM/BSE micrographs of Figures 15 and 16, as well as the elemental Al map of Figure 15 and the EDS concentration profile of Figure 16, show a disappearance of the Co_3Al part of the matrix over a depth of about 100 µm. In addition to the Al concentration profiles, this evidences an Al diffusion towards the oxidation front. This Al movement allows for forming and maintaining the Al-involving complex oxide and the alumina sublayer, which allows the alloy to oxidize slowly, in a similar way as NACT5.

3.9. Oxide Scale Comparison Between the Three Alloys

The previous surface and cross-sectional observations of the oxide scales can be summarized by separating, on the one hand, the CACT5 alloy, and on the other hand, the NACT5 and CACT10 alloys. CACT5 oxidized rapidly and was finally covered by a thick duplex alumina-free oxide scale in which Co took part much more than Al. In contrast, the NACT5 and CACT10 alloys oxidized more slowly thanks to the formation of a protective scale made of a continuous spinel oxide (either $NiAl_2O_4$ or $CoAl_2O_4$) and an innermost continuous Al_2O_3 alumina scale. The oxidized states of the NACT5 and CACT10 alloys are, thus, similar and responsible for their acceptable oxidation behaviors, and both are totally different from the CACT5 alloy's, which did not benefit from good protection against oxidation.

The transition from catastrophic oxidation (a thick outermost MO scale and a thick innermost complex oxide principally mixing MO and MAl_2O_4 with M=Co or Ni, here observed only for M=O) to an acceptable oxidation resistance (outermost continuous MAl_2O_4 ant innermost continuous Al_2O_3) occurs across a threshold Al content between 5 wt.% and 10 wt.% for a TaC-containing cobalt alloy, while, if it exists, such an Al threshold should be lower than 5 wt.%. As for chromium-containing alloys, this difference is found between the ease of Al diffusion in a nickel matrix compared to that in a cobalt matrix.

3.10. Summary and General Commentaries

Thus, removing all chromium and replacing it with aluminum does not affect the population of tantalum carbides, which are still script-like shaped and mixed with the periphery of matrix dendrites. However, we mention that additional rare coarse TaC are present, seemingly of a pre-eutectic nature (CACT5 alloy), and that the script eutectic TaCs are slightly modified in the CACT10 alloy, the matrix of which becomes double-phased. Concerning the strengthening effect of TaC, no significant difference is expected. In contrast, the matrix of the cobalt alloys is possibly influenced by the introduction of too much aluminum, as beyond a threshold between 5 and 10 wt.% Al, the matrix evolution may itself have consequences on mechanical properties at high temperatures (creep resistance), but also at ambient temperature (machinability), and further investigation concerning this point will be carried out. Concerning oxidation resistance, it is clear that the alloys are not really alumina-forming while they are chromia-forming with 30 wt.% Cr. Nevertheless, the behaviors in the hot-oxidation nickel alloy with 5 wt.% Al and the cobalt alloy with 10 wt.% Al are promising at this 1200 °C elevated temperature, with parabolic mass gain (no flattening at high durations characteristic of chromia volatilization), and despite the absence of oxide loss, the parabolic constants (about 40×10^{-12} g^2 cm^{-4} s^{-1}) are lower than those for a chromia-forming Ni-30 wt.% Cr in the same conditions ($\cong 70 \times 10^{-12}$ g^2 cm^{-4} s^{-1}). This can be improved if a new enrichment (e.g., 15 wt.% Al) allows the oxide scale to be mainly of alumina. But one must be careful, since it was seen here that the introduction of Al in high amount may destabilize the matrix if its Al solubility is exceeded (e.g., CACT10). Anyway, the microstructures and oxidation behaviors observed in this work allow for considering that this research method is interesting to deepen knowledge and can lead to new alloys with new properties that are potentially interesting.

4. Conclusions

Generally, superalloys which are reinforced by primary carbides to resist creep at high temperatures contain chromium for resisting hot oxidation. Using—in such carbide-strengthened superalloys—aluminum instead of chromium in this role can be an interesting change. This work aimed to investigate the microstructural consequences and the potential

benefits for the hot oxidation behavior of {Cr by Al} replacement in TaC-strengthened model superalloys based on cobalt or based on nickel. It was, thus, discovered that:

- TaC is the single carbide phase present in all alloys if the Ta and C atomic contents are close to one another (already true in Cr-containing Co alloys, but not true in Ni alloys, in which chromium carbides are also present).
- The TaC nature (eutectic with matrix) and morphology (script-like) are the same as those in the Cr-containing alloys, however with a tendency to have more additional pre-eutectic compact TaC.
- Raising the Al content to 10 wt.% induces a matrix change for the TaC–cobalt alloy with the appearance of the second matrix phase Co_3Al
- To preserve the TaC-containing Co alloy from catastrophic oxidation, 5 wt.% is not enough. The threshold to exceed for acceptable oxidation behavior is between 5 and 10 wt.%; 5 wt.% is over this threshold for the TaC-containing Ni alloy
- By respecting the threshold above, this is still not a real alumina-forming behavior, since a spinel oxide at least as thick as the alumina scale forms too; however, the mass gain kinetics are interesting, as they are similar to those of chromia-forming alloys

Further investigations will first address the determination of ideal Al content for TaC-containing cobalt alloys, still allowing the {spinel + alumina} double continuous layer and the lack of appearance of the intermetallic Co_3Al phase in the matrix, which may be potentially deleterious for the mechanical properties (notably in terms of machinability and toughness). A second objective is increasing the Al content of the TaC-containing Ni alloy beyond a threshold (to define) to allow a proper alumina-forming behavior. Another extension of this work is also to mechanically test the alloys to know how their creep resistance develops with such fundamental changes in their chemical composition.

Funding: This research received no external funding.

Data Availability Statement: Data is contained within the article.

Acknowledgments: The author wishes thanking Lionel Aranda for his assistance for the thermogravimetry tests.

Conflicts of Interest: The author declares no conflicts of interest.

References

1. Donachie, M.S.; Donachie, S.J. *Superalloys: A Technical Guide*, 2nd ed.; ASM International: Phoenix, AZ, USA, 2002.
2. Young, D.J. *High Temperature Oxidation and Corrosion of Metals*; Elsevier: Amsterdam, The Netherlands, 2008.
3. Sims, C.T.; Hagel, W.C. *The Superalloys*; Wiley-Interscience: New York, NY, USA, 1972.
4. Durand–Charre, M. *The Microstructure of Superalloys*; CRC Press: Boca–Raton, FL, USA, 1997.
5. Bradley, E.F. *Superalloys: A Technical Guide*; ASM International: Phoenix, AZ, USA, 1988.
6. Beltran, A.M.; Sims, C.T.; Wagenheim, N.T. The high-temperature properties of Mar-M alloy 509. *J. Metals* **1969**, *21*, 39–47. [CrossRef]
7. Potter, A.; Sumner, J.; Simms, N.J. The role of superalloy precipitates on the early stages of oxidation and type II hot corrosion. *Mater. High Temp.* **2018**, *35*, 236–242. [CrossRef]
8. Kofstad, P. *High Temperature Corrosion*; Elsevier Applied Science: London, UK, 1988.
9. Grudzien-Rakoczy, M.; Rakoczy, L.; Cygan, R.; Kromka, F.; Pirowski, Z.; Milkovoic, O. Fabrication and characterization of the newly developed superalloys based on Inconel 740. *Materials* **2020**, *13*, 2362. [CrossRef] [PubMed]
10. Makineni, S.K.; Samanta, A.; Rojhirunsakool, T.; Alam, T.; Nithin, B.; Singh, A.K.; Banerjee, R.; Chattopadhyay, K. A new class of high strength high temperature cobalt based γ–γ' Co-Mo-Al alloys stabilized with Ta addition. *Acta Mater.* **2015**, *97*, 29–40. [CrossRef]
11. Chen, Y.; Wang, C.; Ruan, J.; Yang, S.; Omori, T.; Kainuma, R.; Ishida, K.; Han, J.; Lu, Y.; Lu, X. Development of low-density γ/γ' Co–Al–Ta-based superalloys with high solvus temperature. *Acta Mater.* **2020**, *188*, 652–664. [CrossRef]

12. Nithin, B.; Samanta, A.; Makineni, S.K.; Alam, T.; Pandey, P.; Singh, A.K.; Banerjee, R.; Chattopadhyay, K. Effect of Cr addition on γ–γ′ cobalt-based Co-Mo-Al-Ta class of superalloys: A combined experimental and computational study. *J. Mater. Sci.* **2017**, *52*, 11036–11047. [CrossRef]
13. Senkov, O.N.; Isheim, D.; Seidman, D.N.; Pilchak, A.L. Development of a refractory high entropy superalloy. *Entropy* **2016**, *18*, 102. [CrossRef]
14. Pickering, E.J.; Christofidou, K.A.; Stone, H.J.; Jone, N.G. On the design and feasibility of tantalum-base superalloys. *J. Alloys Compds.* **2019**, *804*, 314–321. [CrossRef]
15. Lu, Z.; Xu, Y.; Hu, Z. Low cycle fatigue behavior of a directionally solidified cobalt base superalloy. *Mater. Sci. Eng. A* **1999**, *270*, 162–169. [CrossRef]
16. Bala, P.; Morgiel, J.; Cios, G.; Wieczerzak, K.; Tokarski, T. Ni-Cr-Ta-Al-C complex phase alloy—Design, microstructure and properties. *Mater. Sci. Eng. A* **2018**, *711*, 99–108. [CrossRef]
17. Shyr, F.S. Study on the high-temperature oxidation of molten aluminum-magnesium alloys. *Kyangye* **1997**, *41*, 72–76.
18. Schwerdtfeger, J.; Koerner, C. Selective electron beam melting of Ti-48Al-2Nb-2Cr: Microstructure and aluminum loss. *Intermetallics* **2014**, *49*, 29–35. [CrossRef]
19. Oleksiak, B.; Blacha, L.; Siwiec, G.; Smalcerz, A. Loss of aluminium during the process of Ti-Al alloy melting in VIM furnace. *Adv. Mater. Res.* **2014**, *1036*, 422–427. [CrossRef]
20. Jepson, S.; Kim, H. Calculated aluminum oxidation rates during rotary furnace melting through flue gas analysis—Part two. In *Light Metals*; Williams, E., Ed.; Springer: Cham, Switzerland, 2016; pp. 767–771. [CrossRef]
21. Smalcerz, A.; Blacha, L.; Labaj, J. Aluminium loss during Ti-Al-X alloy smelting using the VIM technology. *Arch. Foundry Eng.* **2021**, *21*, 11–17. [CrossRef]
22. Fenocchio, L.; Gambaro, S.; Cacciamani, G. Critical assessment of phase equilibria in the Al-Co-Ta and Al-Ni-Ta systems. *J. Phase Equilib. Diffus.* **2024**, *45*, 986–1010. [CrossRef]

Disclaimer/Publisher's Note: The statements, opinions and data contained in all publications are solely those of the individual author(s) and contributor(s) and not of MDPI and/or the editor(s). MDPI and/or the editor(s) disclaim responsibility for any injury to people or property resulting from any ideas, methods, instructions or products referred to in the content.